High Pt-Mass Activity of Pt_1^{IV}/β-MnO_2 Surface for Low-Temperature Oxidation of CO under O_2-Rich Conditions

Takeshi Nagata,[a] Akira Oda,[a,b]* Yuta Yamamoto,[c] Risa Ichihashi,[a] Kyoichi Sawabe,[a,b] Atsushi Satsuma[a,b]*

[a]Department of Materials Chemistry, Graduate School of Engineering, Nagoya University, Furo-cho, Chikusa-ku, Nagoya 464-8603, Japan.

[b]Elements Strategy Initiative for Catalysts and Batteries (ESICB) Kyoto University, Katsura-ku, Kyoto 615-8520, Japan.

[c] Institute of Materials and Systems for Sustainability, Nagoya University, Nagoya 464-8603, Japan.

ABSTRACT: A Pt-based CO oxidation catalyst that works even at low temperatures is desirable for industrial applications; however, its development is highly challenging because of Pt's high affinity toward CO. Here, we develop a Pt^{IV} single-atom/β-MnO_2 composite metal-oxide surface (Pt_1^{IV}/β-MnO_2). Single Pt^{IV} sites were stably formed on the high surface β-MnO_2 by strong interaction with Mn^{IV} defect sites. The resulting Pt^{IV}–O–Mn^{IV} local structures served the lattice oxygens as an oxidant to catalyze low-temperature oxidation of CO. Pt_1^{IV}/β-MnO_2 was highly resistant to CO poisoning because of the high-valence state of the Pt^{IV} single-atom sites. Aided by these geometric and electronic features, the CO oxidation was catalyzed with reaction rates of 0.676 and 0.206 $mol_{CO}/h/g_{Pt}$ at 25 ℃ and 0 ℃, respectively, under the O_2-rich conditions (O_2: CO ratio of 66.7). These are record rates in the literature for Pt-based catalyst application for low-temperature CO oxidation under near atmospheric conditions.

KEYWORDS: *low temperature oxidation of CO, Pt single-atom catalyst, heterogeneous catalysis, high surface β-MnO_2 support, near atmospheric reaction*

Catalytic oxidation of CO at low temperatures is one of the important catalytic processes for industrial applications, including exhaust gas purification during the cold start of automobiles, air reforming, hydrogen energy utilization, and removal of CO as an impure gas in storage and transportation processes.[1,2] Although Pt is well known as a key element for designing heterogeneous catalytic oxidation processes, its application for low-temperature oxidation of CO is hindered because of the high affinity of Pt toward CO.[2–4] Only a handful of Pt-based catalysts have been successfully applied to catalytic CO oxidation below 30 °C.[5–7] However, these catalysts are characterized by high catalytic activity only under dilute oxygen conditions (O_2/CO = 1.0–1.7).[5-7] It is desirable to develop a Pt-based catalyst that shows high catalytic activity under an excess of oxygen assuming the atmospheric applications.

Single-atom catalysts (SACs) have attracted much attention because of their unique catalytic properties originating from atomicity.[8–12] Noble metal-based SACs are attractive also from the viewpoint of precious metal conservation because they maximize the atom efficiency of expensive noble metal elements. The catalytic performance of SACs is affected by the electronic state and local structure of the atomic active sites.[10,13,14] Numerous studies have thus tried to create the outstanding catalytic property of the SACs based on the concept of *coordination environment regulation*.[8–11,15] In 2011, Zhang et al. succeeded, for the first time, in designing a Pt-based SAC that catalyzes CO oxidation at low temperatures.[5] The active site was identified as the $Pt^{\delta+}$ single-atom site that was generated through a strong interaction between Pt atom and an Fe-defect site over the FeO_x support under H_2-treatment. The $Pt^{\delta+}$ site has a low CO affinity because of the relatively high oxidation state of Pt and thereby exhibited an extremely high reaction rate (0.435 $mol_{CO}/h/g_{Pt}$) at 27 ℃. The significance of the interaction between the single Pt atom and the reducible metal oxide has also been pointed out for the low-temperature oxidation of CO. Nie et al. reported that Pt single-atoms that are immobilized on CeO_2 (Pt_1/CeO_2) activate the lattice O of CeO_2 and catalyze the CO oxidation using the lattice O and related defect sites.[16] The apparent activation energy was lower by 35 kJ/mol than that of the Pt-based SACs with redox-inactive metal-oxide support.[17]

Here, we report a high-valence Pt^{IV} single-atom/β-MnO_2 composite oxide surface with the highest CO oxidation rates at 25 ℃ and 0 ℃, respectively, under the O_2-rich conditions (O_2: CO ratio of 66.7). Mn is the 12th most abundant element in the earth's crust, and its oxide (MnO_2) has been widely studied in the field of environmental purification systems as an adsorbent catalyst.[18–22] MnO_2 has α, β, γ, δ, and λ crystal structures, and the applications related to the formation of O defects due to the high redox activity of Mn are well known. Among them, β-MnO_2 exhibits a high efficiency of the oxygen defect formation on the surface.[23] It is expected that this material has potential as the support for the preparation of the single Pt site with high activity toward low-temperature oxidation of CO. However, to our knowledge, no Pt-based SAC has been synthesized using β-MnO_2 as support and applied to CO oxidation. In this study, Pt was atomically supported on high surface area β-MnO_2 by the simplest procedure, and we successfully designed the Pt-based SAC with both resistance to CO poisoning and high catalytic activity for low-temperature CO oxidation, allowing the catalytic applications at 0 and 25 ℃ with record reaction rates under the O_2-rich conditions.

We started with the synthesis of the high-surface-area β-MnO_2. The synthesis of β-MnO_2 was performed by a simple synthesis method using sodium permanganate and manganese sulphate as raw materials, according to a previous report.[23] The synthesized β-MnO_2 provided an X-ray diffraction (XRD) pattern derived from rutile-type β-MnO_2 (tetragonal, $P4_2/mnm$: **Fig. S1**). The particles had a

protruding surface with a specific surface area of 150 m^2/g (**Fig. S2, and Table S1**). Using the obtained high-surface β-MnO_2 as support, β-MnO_2-supported Pt single-atom (Pt_1/β-MnO_2) was then prepared. Our preparation procedure is the simplest; the air-stable Pt_1/β-MnO_2 could be obtained only by impregnation of the β-MnO_2 with an aqueous solution containing 0.2 wt% Pt, followed by drying and calcination in air. **Fig. 1a** presents the Cs-corrected high-angle annular dark-field scanning transmission electron microscopy (HAADF-STEM) image of Pt_1/β-MnO_2. The Pt species were atomically-dispersed over the β-MnO_2 surface. Additional HAADF-STEM images are also given in **Fig. S3**. The Pt_1/β-MnO_2 gave X-ray photoelectron spectroscopy (XPS) signals derived from Pt^{IV} $4f_{5/2}$ and Pt^{IV} $4f_{7/2}$ at 78.1 and 74.8 eV (**Fig. 1b**).[24,25] No signals of Pt^{II} or Pt^0 were observed. Therefore, the Pt single-atoms on the β-MnO_2 surface were in the Pt^{IV} oxidation state. This high-valence state was also supported by the Pt L_{III}-edge X-ray absorption near-edge structure (XANES) spectrum (**Fig. 1c**), where the white-line intensity of the XANES spectrum of Pt_1/β-MnO_2 was higher than that of bulk PtO_2.

We next analyzed the extended X-ray absorption fine structure (EXAFS) in the Pt L_{III}-edge XAFS spectrum, investigating the geometric feature of the Pt^{IV} single-atom site. First, the $k^3\chi(k)$ function was extracted from the EXAFS region, and the $3.0 < k < 12.0$ $Å^{-1}$ region was Fourier transformed (**Fig. 2a**). The obtained Fourier transform EXAFS (FT-EXAFS) spectrum gave peaks in the 1.6 and 2–3 Å regions, respectively. Considering the HAADF-STEM image, the former can be attributed to Pt–O backscattering, and the latter to Pt–(O)–Mn and Pt–(O–Mn)–O backscattering. To verify the validity of these assignments, the $k^3\chi(k)$ function was analyzed through a wavelet transform (**Fig. 2b**). In the wavelet transform EXAFS (WT-EXAFS), Pt–O backscattering was observed at R = 1.6 Å and k = 7 $Å^{-1}$. In addition, two types of backscattering were observed at R = 2–3 Å, k = 4 $Å^{-1}$, and R = 2–3 Å, k = 7 $Å^{-1}$. These could not be assigned as Pt–Pt backscattering because their k values are out of the range of Pt–Pt backscattering (refer to Pt–Pt backscattering in the WT-EXAFS of Pt-foil and PtO_2: **Fig. 2c, d**). Undoubtedly, the lobes observed at R = 2–3 Å, k = 4 $Å^{-1}$ and R = 2–3 Å, k = 7 $Å^{-1}$ could be attributed to Pt–(O–Mn)–O and Pt–(O)–Mn backscattering, respectively. The direct observations of the Pt–(O–Mn)–O and Pt–(O)–Mn backscattering indicate a strong interaction between the Pt^{IV} single-atoms and β-MnO_2 via the formation of the Pt–O–Mn bonds. The coordination number of nearest oxygen was evaluated as 6.1±1.3 by EXAFS fitting (**Table S2** and **Fig. S4**), suggesting the octahedra Pt_1O_6 geometry on the β-MnO_2 surface.

The above HAADF-STEM, XPS, XANES, FT-EXAFS, and WT-EXAFS results indicates that the β-MnO_2 surface created Pt^{IV} single-atom sites with the geometric and electronic features shown in **Fig. 3**: Pt_1^{IV}/β-MnO_2. Here, we schematically described the Pt_1^{IV} single site coordinated with only lattice oxygen of β-MnO_2 surface as the most plausible model. We now demonstrate its remarkable activity of toward low-temperature oxidation of CO.

CO oxidation tests were carried out on Pt_1^{IV}/β-MnO_2 under O_2-rich conditions (0.3% CO–20% O_2–79.7% Ar; O_2/CO= 66.7; GHSV= 240 $L/g_{cat}/h$), assuming the practical application under atmosphere. The Pt_1^{IV}/β-MnO_2 catalyzed the CO oxidation with reaction rates of 0.676 $mol_{CO}/h/g_{Pt}$ at 25 ℃ (**Table 1, entry 1**), which is almost equivalent with the reaction rate reported for Pt_1/FeO_x[5] at 27 ℃ under the O_2-dilute conditions (**Table 1, entry 6**). Our catalyst well worked also under such the dilute O_2 condition, exhibiting the reaction rate of 0.410 $mol_{CO}/h/g_{Pt}$ at 25 ℃ (**Table 1, entry 2**). By contrast to the Pt_1^{IV}/β-MnO_2 catalyst, no reaction was observed on the Pt-free β-MnO_2 support under the same conditions; the CO_2 yield was less than the detectable amount. Thus, the low-temperature catalytic activity of Pt_1^{IV}/β-MnO_2 originates from the reaction field formed by the interaction between the Pt^{IV} single-atom and the β-MnO_2 surface (**Fig. 3**). This reactive-center hypothesis was further supported by the dependence of the CO oxidation rate on the Pt loading (**Fig. 4** and **Table S3**); the catalyst with a loading higher than 0.2 wt% showed a low reaction rate per gram of Pt. Although the dispersion of Pt species is high as evidenced by no diffraction peak of bulk PtO_2 (**Fig. S5**) benefiting from the strong interaction between PtO_x and MnO_2 surface, STEM images showed the aggregation of the supported PtO_x species over the higher-loading samples (**Fig. S6**). As the aggregated PtO_x clusters increased with the Pt loading, the catalytic activity for CO oxidation became lower.

Although Pt_1/CeO_2 and Pt_1/FeO_x are well known as the low temperature CO oxidation catalysts, there has been no report of evaluation of the low-temperature CO oxidation activity under an O_2-rich condition. Therefore, we cannot judge whether our catalyst is specific or not in the present stage. We then prepared Pt_1/CeO_2 and Pt_1/Fe_2O_3 catalysts, and evaluated their catalytic activities under the O_2-rich conditions. Despite the atomic-dispersion of Pt sites (**Fig. S7**), Pt_1/CeO_2 and Pt_1/FeO_x showed negligible catalytic activity (**Table 1, entries 4 and 5**). Based on these data, we can reasonably claim that Pt_1^{IV}/β-MnO_2 is an unusual Pt-based SAC that is active for low-temperature CO oxidation under the presence of an excess of O_2.

Surprisingly, Pt_1^{IV}/β-MnO_2 functions as a catalyst even at 0 ℃under the O_2-rich condition, providing a reaction rate of 0.206 $mol_{CO}/h/g_{Pt}$ (**Table 1, entry 3**), which is the first example for the Pt-based catalyst. Consistently, our kinetic experiments showed an apparent activation energy ($^{ap}E_a$) of only 29.1 kJ/mol^{-1} for CO oxidation over Pt_1^{IV}/β-MnO_2 (**Fig. S8**). This value is 13.4–48.4 kJ mol^{-1} lower than the $^{ap}E_a$ of the Pt-based SACs in the published literature,[16,17] supporting the high activity of Pt_1^{IV}/β-MnO_2 toward low-temperature CO oxidation under an excess of O_2.

To gain a mechanistic insight into the notable catalytic oxidation process observed on Pt_1^{IV}/β-MnO_2, the dependencies of the CO oxidation rate on the CO and O_2 pressures were investigated (**Fig. 5**). The Pt_1^{IV}/β-MnO_2 catalyst showed negligible dependency on CO-pressure (**Fig. 5a**). The reaction order of CO was estimated as +0.11. These are indicative that Pt_1^{IV}/β-MnO_2 was highly resistant to CO poisoning.[3,17] It expected to originate from the high-valence

state of Pt^{IV} single-atom site. A positive reaction order (+0.36) was observed for the O_2 pressure dependency (**Fig. 5b**). This value is extremely low compared with the catalytic reaction over the Pt-based SACs with the redox inactive metal-oxide support, i.e., Pt_1/Al_2O_3,[18] where O_2 reaction order of +1.6 was reported. This comparison suggests involvement of the lattice O of the β-MnO_2 support in the low-temperature CO oxidation over the Pt_1^{IV}/β-MnO_2 catalyst. Consistently, Pt single-atom sites over a reducible metal-oxide support have been reported to catalyze CO oxidation via the Mars–van Krevelen mechanism.[3,16,29]

Single metal sites are often reported to diffuse on the support during a reaction with the formation of a new dynamic reactive center.[26,27] However, such reactive-center dynamics were not observed in the present system. **Fig. S9** shows The Pt L_{III}-edge XAFS data for the Pt_1^{IV}/β-MnO_2 catalyst under the reaction conditions. The white-line intensity of XANES scarcely changed upon the reaction (**Fig. S9a**), indicating that the high-valence state of Pt^{IV} was stable under the catalytic operation. In FT- and WT-EXAFS, no Pt–Pt backscattering was observed (**Fig. S9b, c**). Both Pt–(O)–Mn and Pt–(O–Mn)–O backscattering were maintained under the CO oxidation catalysis. Accordingly, Pt_1^{IV} was stable on β-MnO_2 surface via the strong Pt–O–Mn bonds, working as an active site for the low-temperature CO oxidation.

In summary, we have successfully designed Pt_1^{IV}/β-MnO_2 for low-temperature CO oxidation under the O_2-rich conditions. The Pt_1^{IV}/β-MnO_2 catalyst showed high CO oxidation rates (0.676 $mol_{CO}/h/g_{Pt}$ at 25 °C and 0.206 $mol_{CO}/h/g_{Pt}$ at 0 °C). The $^{ap}E_a$ was 29.1 kJ mol^{-1}, which was smaller than that of previously reported Pt-based SACs (Pt_1/Al_2O_3[17], Pt_1/CeO_2[16]). The remarkable catalytic activity originated from both the electronic features of Pt_1^{IV}/β-MnO_2. The Pt^{IV}-binding to the β-MnO_2 surface contributes to the activation of the lattice O atoms, enabling lattice-mediated CO oxidation catalysis at low temperatures. Because of the high-valence state of Pt_1^{IV}, the effect of CO poisoning was negligible. The present findings suggest that the precisely controlling the interaction between high-valence Pt^{IV} single-atom and the reducible metal-oxide surface with the low O defect formation energy is an effective approach to create Pt-based CO oxidation catalyst that works well at low temperatures and under near atmospheric conditions.

Conflicts of interest

The authors declare no competing financial interest.

Acknowledgements

This work was supported by a Japan Society for the Promotion of Science (JSPS) Grant-in-Aid for Young Scientists (No. 20K15297), JSPS Grant-in-Aid for Scientific Research (B) (No. 18H01787), and the Foundation of Public Interest of the Tatematsu. Part of this work was managed by ESICB (JPMXP0112101003). XAFS measurements were conducted at BL5S1 of the Aichi Synchrotron Radiation Center, Aichi Science & Technology Foundation (Approval No. 202103056), and at the BL01B1 line of SPring-8 (Proposal Nos. 2021A1165 and 2021B1691).

References

(1) M. Haruta, *Chem. Rec*., 2003, **3**, 75–87.
(2) H. Guan, J. Lin, B. Qiao, X. Yang, L. Li, S. Miao, J. Liu, A. Wang, X. Wang, T. Zhang, *Angew. Chem. Int. Ed*., 2016, **55**, 2820–2824.
(3) N. Zhang, L. Li, R. Wu, L. Song, L. Zheng, G. Zhang, H. He, *Catal. Sci. Technol*., 2019, **9**, 347–354.
(4) E. J. Peterson, A. T. DeLaRiva, S. Lin, R. S. Johnson, H. Guo, J. T. Miller, J. H. Kwak, C. H. F. Peden, B. Kiefer, L. F. Allard, F. H. Ribeiro, A. K. Datye, *Nat. Commun*., 2014, **5**, 1–11.
(5) B. Qiao, A. Wang, X. Yang, L. F. Allard, Z. Jiang, Y. Cui, J. Liu, J. Li, T. Zhang, *Nat. Chem.*, 2011, **3**, 634–641.
(6) S. Gatla, D. Aubert, G. Agostini, O. Mathon, S. Pascarelli, T. Lunkenbein, M. G. Willinger, H. Kaper, *ACS Catal.*, 2016, **6**, 6151–6155.
(7) J. Li, Y. Tang, Y. Ma, Z. Zhang, F. Tao, Y. Qu, *ACS Appl. Mater. Interfaces*., 2018, **10**, 38134–38140.
(8) H. Jeong, S. Shin, H. Lee, *ACS Nano*., 2020, **14**, 14355–14374.
(9) S. K. Kaiser, Z. Chen, D. Faust Akl, S. Mitchell, J. Pérez-Ramírez, *Chem. Rev*., 2020, **120**, 11703–11809.
(10) R. Lang, X. Du, Y. Huang, X. Jiang, Q. Zhang, Y. Guo, K. Liu, B. Qiao, A. Wang, T. Zhang, *Chem. Rev.*, 2020, **120**, 11986–12043.
(11) Z. Li, S. Ji, Y. Liu, X. Cao, S. Tian, Y. Chen, Z. Niu, Y. Li, *Chem. Rev.*, 2020, **120**, 623–682.
(12) N. Cheng, L. Zhang, K. Doyle-Davis, X. Sun, *Springer Singapore*., 2019, 2.
(13) Y. Ren, Y. Tang, L. Zhang, X. Liu, L. Li, S. Miao, D. Sheng Su, A. Wang, J. Li, T. Zhang, *Nat. Commun*., 2019, **10**, 1–9.
(14) Y. Ma, B. Chi, W. Liu, L. Cao, Y. Lin, X. Zhang, X. Ye, S. Wei, J. Lu, *ACS Catal*., 2019, **9**, 8404–8412.
(15) T. Zhang, *Nano Lett*., 2021, **21**, 9835–9837.
(16) L. Nie, D. Mei, H. Xiong, B. Peng, Z. Ren, X. I. P. Hernandez, A. DeLaRiva, M. Wang, M. H. Engelhard, L. Kovarik, A. K. Datye, Y. Wang, *Science*., 2017, **358**, 1419–1423.
(17) Z. Zhang, Y. Zhu, H. Asakura, B. Zhang, J. Zhang, M. Zhou, Y. Han, T. Tanaka, A. Wang, T. Zhang, N. Yan, *Nat. Commun*., 2017, **8**, 1–10.
(18) R. Yang, Y. Fan, R. Ye, Y. Tang, X. Cao, Z. Yin, Z. Zeng, *Adv. Mater*., 2021, **33**, 1–53.
(19) Z. Sihaib, F. Puleo, J. M. Garcia-Vargas, L. Retailleau, C. Descorme, L. F. Liotta, J. L. Valverde, S. Gil, A. Giroir-Fendler, *Appl. Catal. B Environ*., 2017, **209**, 689–700.
(20) J. Wang, P. Zhang, J. Li, C. Jiang, R. Yunus, J. Kim, *Environ. Sci. Technol.*, 2015, **49**, 12372–12379.
(21) S. Rong, P. Zhang, Y. Yang, L. Zhu, J. Wang, F. Liu, *ACS Catal*., 2017, **7**, 1057–1067.
(22) X. Liao, Y. Zhao, C. Liu, X. Li, Y. Sun, K. Kato, M. Yamauchi, Z. Jiang, *J. Energy Chem*., 2021, **62**, 136–144.
(23) E. Hayashi, Y. Yamaguchi, K. Kamata, N. Tsunoda, Y. Kumagai, F. Oba, M. Hara, *J. Am. Chem. Soc*., 2019, **141**, 899–900.
(24) K. Ding, A. Gulec, A. M. Johnson, N. M. Schweitzer, G. D. Stucky, L. D. Marks, P. C. Stair, *Science*., 2015, **350**, 189–192.
(25) D. Yan, J. Chen, H. Jia, *Angew. Chem. Int. Ed*., 2020, **59**, 13562–13567.
(26) L. DeRita, J. Resasco, S. Dai, A. Boubnov, H. V. Thang, A. S. Hoffman, I. Ro, G. W. Graham, S. R. Bare, G. Pacchioni, X. Pan, P. Christopher, *Nat. Mater*., 2019, **18**, 746–751.

(27) C. Paolucci, I. Khurana, A. A. Parekh, S. Li, A. J. Shih, H. Li, J. R. Di Iorio, J. D. Albarracin-caballero, A. Yezerets, J. T. Miller, W. N. Delgass, F. H. Ribeiro, W. F. Schneider, R. Gounder, *Science*., 2017, **903**, 898–903.
(28) M. Moses-Debusk, M. Yoon, L. F. Allard, D. R. Mullins, Z. Wu, X. Yang, G. Veith, G. M. Stocks, C. K. Narula, *J. Am. Chem. Soc*., 2013, **135**, 12634–12645.
(29) C. Wang, X. K. Gu, H. Yan, Y. Lin, J. Li, D. Liu, W. X. Li, J. Lu, *ACS Catal*., 2017, **7**, 887–891.

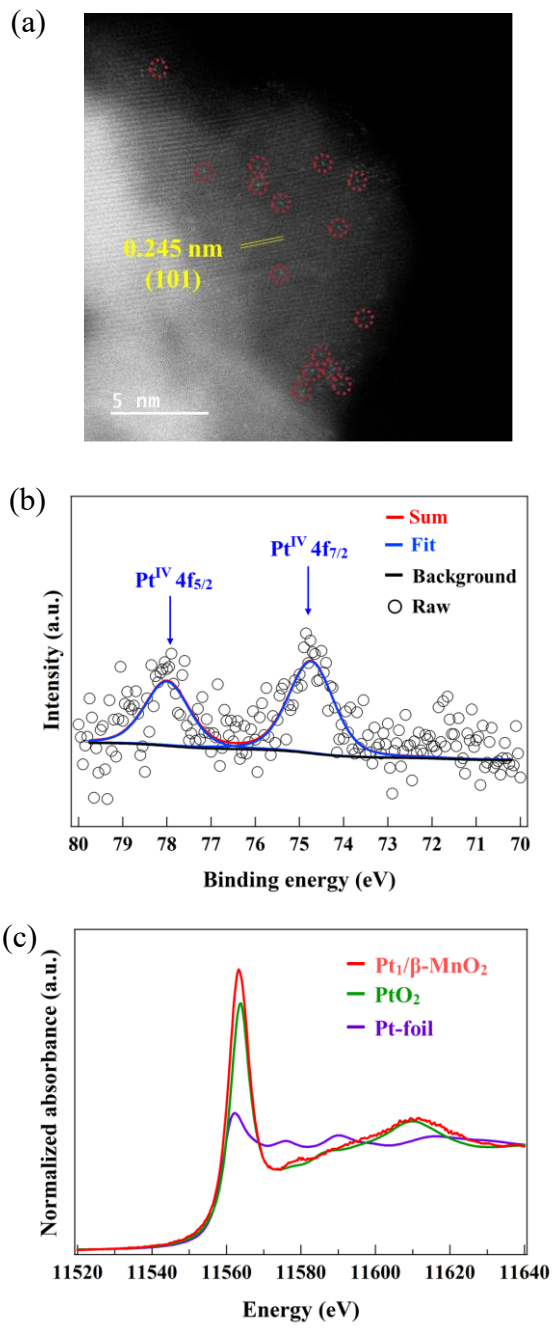

Fig. 1 (a) HAADF-STEM image of Pt_1/β-MnO_2, where the Pt single-atom sites are indicated by red circles. (b) Pt 4f XPS spectrum and (c) Pt L_{III}-edge XANES spectrum. The XANES data for PtO_2 and Pt-foil are also given for comparison.

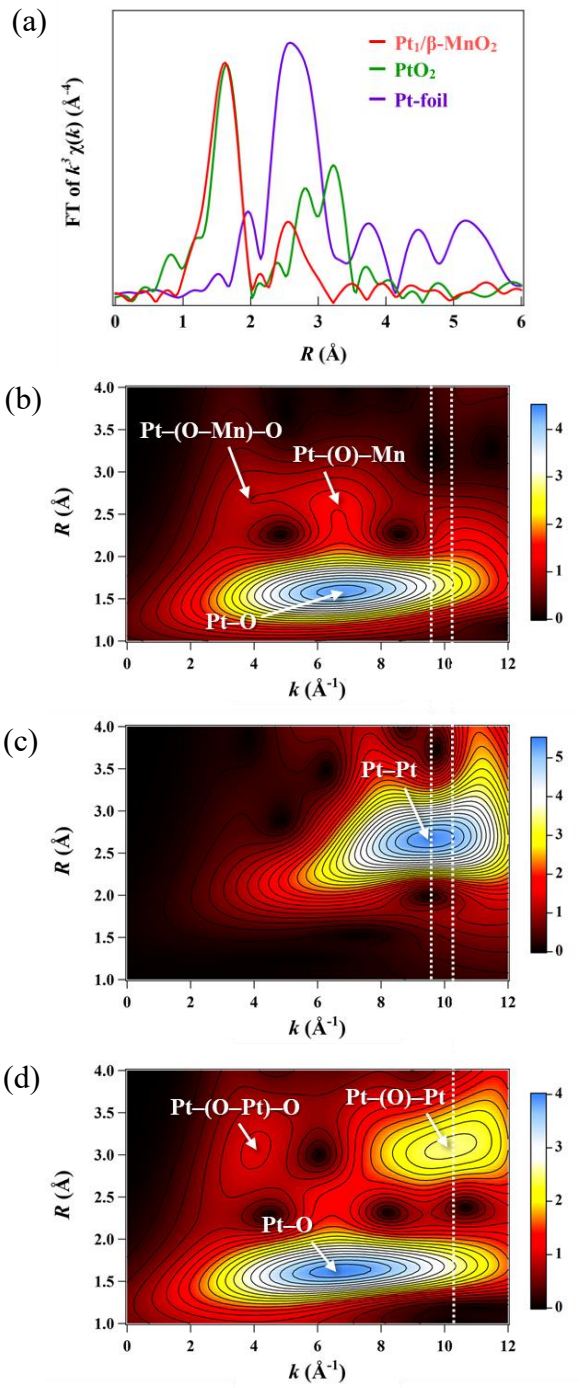

Fig. 2 (a) Pt L_{III}-edge FT-EXAFS of Pt_1/β-MnO_2, Pt-foil, and PtO_2. (b-d) WT-EXAFS of (b) Pt_1/β-MnO_2, (c) Pt-foil, and (d) PtO_2. The *k*-ranges where the Pt–Pt backscattering was observed for PtO_2 and Pt-foil are indicated by white dotted lines.

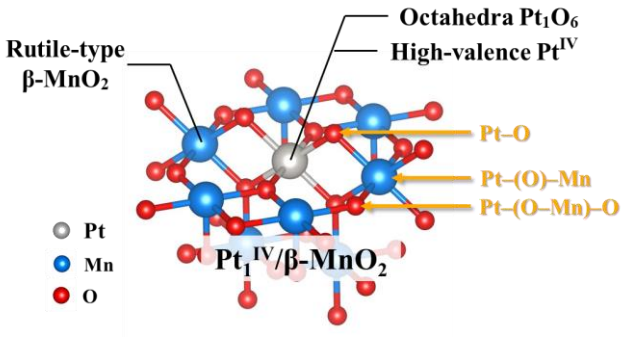

Fig. 3 Schematic view of the Pt^{IV} single-atom site created on the β-MnO_2 surface. The geometric and electronic features are summarized here.

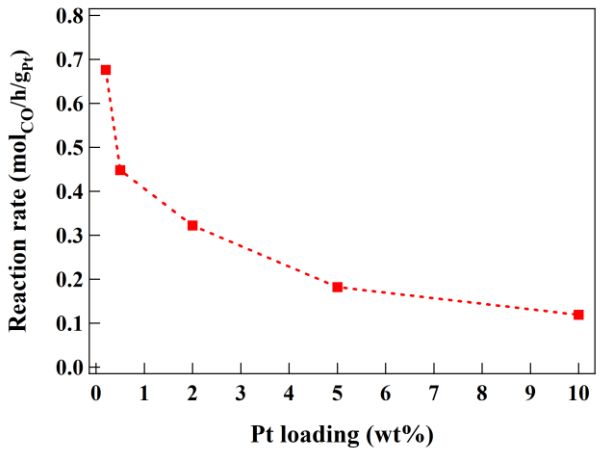

Fig. 4 Reaction rates for CO oxidation at 25 ℃ over Pt/β-MnO_2 catalysts with Pt loadings of 0.2 wt%, 0.5 wt% 2.0 wt%, 5.0 wt%, and 10.0 wt%. Reaction condition: 0.3% CO–20% O_2–79.7% Ar, with a total flow rate of 400 mL/min (240 L/g_{cat}/h), 100 mg catalyst.

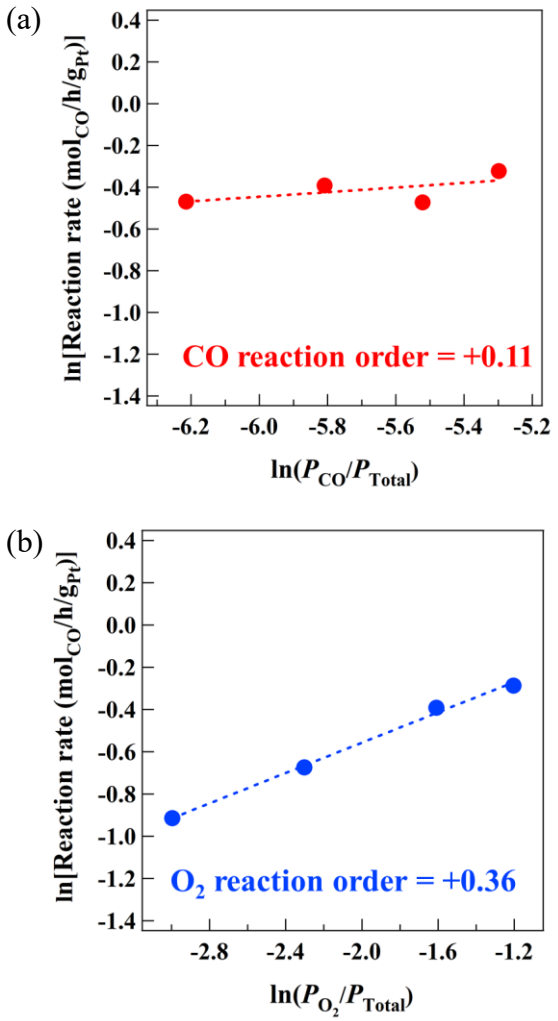

Fig. 5 Dependencies of the reaction rates of CO oxidation over Pt_1^{IV}/β-MnO_2 on the (a) CO pressure (at 25 ℃), and (b) O_2 pressure (at 25 ℃). Reaction conditions: *x*% CO–20% O_2–(80-*x*) % Ar for (a) and 0.3% CO–*y*% O_2–(99.7-*y*) % Ar for (b), with total flow rate of 400 mL/min (240 L/g_{cat}/h), 100 mg catalyst (*x*= 0.2, 0.3, 0.4, 0.5; *y*= 5, 10, 20, 30).

Table 1. Summary of the reaction rates of CO oxidation at low temperature.

entry	catalyst	Pt loading (wt%)	reaction temperature (℃)	gas composition	O_2/CO ratio	GHSV ($L/g_{cat}/h$)	reaction rate ($mol_{CO}/h/g_{Pt}$)	ref.
1	$Pt_1^{IV}/\beta\text{-}MnO_2$	0.2	25	0.3% CO–20% O_2–79.7% Ar	66.7	240	0.676	This work
2	$Pt_1^{IV}/\beta\text{-}MnO_2$	0.2	25	1% CO–1% O_2–98% Ar	1	240	0.410	This work
3	$Pt_1^{IV}/\beta\text{-}MnO_2$	0.2	0	0.3% CO–20% O_2–79.7% Ar	66.7	240	0.206	This work
4	Pt_1/Fe_2O_3	0.2	25	0.3% CO–20% O_2–79.7% Ar	66.7	240	0.042	This work
5	Pt_1/CeO_2	0.2	25	0.3% CO–20% O_2–79.7% Ar	66.7	240	0	This work
6	Pt_1/FeO_x	0.17	27	1% CO–1% O_2–98% Ar	1	19	0.435	[5]

Table of Contents

We successfully developed a Pt^{IV} single-atom/β-MnO_2 composite metal-oxide surface ($Pt_1^{IV}/\beta\text{-}MnO_2$) capable of catalyzing CO oxidation with the record reaction rates of 0.676 and 0.206 $mol_{CO}/h/g_{Pt}$ at 25 °C and 0 °C, respectively, under the O_2-rich conditions (O_2:CO ratio of 66.7).